

# OBSERVATION OF VERY HIGH ENERGY GAMMA RAYS FROM HESS J1804–216 WITH CANGAROO-III TELESCOPES

Y. HIGASHI,<sup>1</sup> H. KUBO,<sup>1</sup> T. YOSHIDA,<sup>2</sup> R. ENOMOTO,<sup>3</sup> T. TANIMORI,<sup>1</sup> P. G. EDWARDS,<sup>6</sup> T. NAITO,<sup>9</sup> G. V. BICKNELL,<sup>4</sup> R. W. CLAY,<sup>5</sup> S. GUNJI,<sup>7</sup> S. HARA,<sup>8</sup> T. HARA,<sup>9</sup> T. HATTORI,<sup>10</sup> S. HAYASHI,<sup>11</sup> Y. HIRAI,<sup>2</sup> K. INOUE,<sup>7</sup> S. KABUKI,<sup>1</sup> F. KAJINO,<sup>11</sup> H. KATAGIRI,<sup>12</sup> A. KAWACHI,<sup>10</sup> T. KIFUNE,<sup>3</sup> R. KIUCHI,<sup>3</sup> J. KUSHIDA,<sup>10</sup> Y. MATSUBARA,<sup>13</sup> T. MIZUKAMI,<sup>1</sup> Y. MIZUMOTO,<sup>14</sup> R. MIZUNIWA,<sup>10</sup> M. MORI,<sup>3</sup> H. MURAISHI,<sup>15</sup> Y. MURAKI,<sup>13</sup> T. NAKAMORI,<sup>1</sup> S. NAKANO,<sup>1</sup> D. NISHIDA,<sup>1</sup> K. NISHIJIMA,<sup>10</sup> M. OHISHI,<sup>3</sup> Y. SAKAMOTO,<sup>10</sup> A. SEKI,<sup>10</sup> V. STAMATESCU,<sup>5</sup> T. SUZUKI,<sup>2</sup> D. L. SWABY,<sup>5</sup> G. THORNTON,<sup>5</sup> F. TOKANAI,<sup>7</sup> K. TSUCHIYA,<sup>1</sup> S. WATANABE,<sup>1</sup> Y. YAMADA,<sup>11</sup> E. YAMAZAKI,<sup>10</sup> S. YANAGITA,<sup>2</sup> T. YOSHIKOSHI,<sup>3</sup> AND Y. YUKAWA<sup>3</sup>

*Draft version August 14, 2019*

## ABSTRACT

We observed the unidentified TeV gamma-ray source HESS J1804–216 with the CANGAROO-III atmospheric Cerenkov telescopes from May to July in 2006. We detected very high energy gamma rays above 600 GeV at the  $10\sigma$  level in an effective exposure of 76 hr. We obtained a differential flux of  $(5.0 \pm 1.5_{\text{stat}} \pm 1.6_{\text{sys}}) \times 10^{-12} (\text{E}/1 \text{ TeV})^{-\alpha} \text{ cm}^{-2} \text{ s}^{-1} \text{ TeV}^{-1}$  with a photon index  $\alpha$  of  $2.69 \pm 0.30_{\text{stat}} \pm 0.34_{\text{sys}}$ , which is consistent with that of the H.E.S.S. observation in 2004. We also confirm the extended morphology of the source. By combining our result with multi-wavelength observations, we discuss the possible counterparts of HESS J1804–216 and the radiation mechanism based on leptonic and hadronic processes for a supernova remnant and a pulsar wind nebula.

*Subject headings:* gamma rays: observations — ISM: individual(HESS J1804–216, G8.7–0.1) — pulsars: individual(PSR B1800–21) — X-rays: individual(Suzaku J1804–2142, Suzaku J1804–2140)

## 1. INTRODUCTION

A Galactic plane survey was performed in 2004 by the H.E.S.S. imaging atmospheric Cerenkov telescope (IACT) with a flux sensitivity of 0.02 crab for gamma rays above 200 GeV (Aharonian et al. 2005a, 2006a). Fourteen new gamma-ray sources were detected at significance levels above  $4\sigma$ , and 11 of the sources either have no counterpart or possible counterparts with significant positional offsets. HESS J1804–216 is one of the bright-

est, and its spectrum is softest in this survey; the flux is about 0.25 crab above 200 GeV with a photon index of  $2.72 \pm 0.06$ . In addition, with a size of  $\sim 22$  arcmin, it is one of the most extended TeV gamma-ray sources. The H.E.S.S. collaboration proposed two possible counterparts: the supernova remnant (SNR) G8.7–0.1 and the young Vela-like pulsar B1800–21. However, the TeV gamma-ray source does not coincide exactly with either of these. G8.7–0.1 appears as a larger circular region with a diameter of  $\sim 50$  arcmin, and the geometric center (Kassim & Weiler 1990b) has a large offset,  $\sim 11$  arcmin, from the centroid of HESS J1804–216 to the northeast, while PSR B1800–21 has an  $\sim 11$  arcmin offset to the west.

After the detection of HESS J1804–216, an SNR, G8.31–0.09, was discovered at radio wavelengths (Brogan et al. 2006) to be located within the error circle of HESS J1804–216, but with a smaller size,  $5' \times 4'$ . *Suzaku* deep observations discovered two new X-ray sources, Suzaku J1804–2142 (hereafter Src1) and Suzaku J1804–2140 (hereafter Src2), that are near the center of HESS J1804–216 (Bamba et al. 2007). *Chandra* also detected these sources (Kargaltsev et al. 2007b). *SWIFT* found three faint X-ray sources in the region of HESS J1804–216 (Landi et al. 2006). One of them is positionally coincident with a bright star, and another could also be associated with a star close to the boundary of the XRT error circle. The other positionally coincides with Suzaku Src2. So, there remain 5 possible counterparts: SNR G8.7–0.1, PSR B1800–21, SNR G8.31–0.09, Suzaku Src1, and Suzaku Src2. We briefly describe these sources in the following paragraphs.

SNR G8.7–0.1: G8.7–0.1 is associated with the W30 complex, which comprises extended radio emission with a number of superposed smaller discrete emission regions

Electronic address: higashi@cr.scphys.kyoto-u.ac.jp

<sup>1</sup> Department of Physics, Kyoto University, Sakyo-ku, Kyoto 606-8502, Japan

<sup>2</sup> Faculty of Science, Ibaraki University, Mito, Ibaraki 310-8512, Japan

<sup>3</sup> Institute for Cosmic Ray Research, University of Tokyo, Kashiwa, Chiba 277-8582, Japan

<sup>4</sup> Research School of Astronomy and Astrophysics, Australian National University, ACT 2611, Australia

<sup>5</sup> School of Chemistry and Physics, University of Adelaide, SA 5005, Australia

<sup>6</sup> CSIRO Australia Telescope National Facility, Narrabri, NSW 2390, Australia

<sup>7</sup> Department of Physics, Yamagata University, Yamagata, Yamagata 990-8560, Japan

<sup>8</sup> Ibaraki Prefectural University of Health Sciences, Ami, Ibaraki 300-0394, Japan

<sup>9</sup> Faculty of Management Information, Yamanashi Gakuin University, Kofu, Yamanashi 400-8575, Japan

<sup>10</sup> Department of Physics, Tokai University, Hiratsuka, Kanagawa 259-1292, Japan

<sup>11</sup> Department of Physics, Konan University, Kobe, Hyogo 658-8501, Japan

<sup>12</sup> Department of Physical Science, Hiroshima University, Higashi-Hiroshima, Hiroshima 739-8526, Japan

<sup>13</sup> Solar-Terrestrial Environment Laboratory, Nagoya University, Nagoya, Aichi 464-8602, Japan

<sup>14</sup> National Astronomical Observatory of Japan, Mitaka, Tokyo 181-8588, Japan

<sup>15</sup> School of Allied Health Sciences, Kitasato University, Sagami-hara, Kanagawa 228-8555, Japan

(Altenhoff et al. 1978; Reich et al. 1984; Handa et al. 1987). Radio recombination-line observations have been used to identify discrete sources as H II regions, and CO observations also show molecular gas to be associated with W30 (Blitz et al. 1982). Ojeda-May et al. (2002) reported that massive star formation may be occurring in molecular clouds in W30. Odegard (1986) and Kassim & Weiler (1990b) clearly established that G8.7–0.1 was an SNR by the detection of a nonthermal extended radio emission. A *ROSAT* observation revealed diffuse X-ray emission only from the northern half of the remnant in the 0.1–2.4 keV band (Finley & Ögelman 1994). The distance to G8.7–0.1 was estimated using several methods. Based on kinematical distances to the H II regions associated with the SNR, the distance was estimated to be  $6 \pm 1$  kpc (Kassim & Weiler 1990b). Finley & Ögelman (1994) pointed out that more recent galactic rotation models applied to the H II regions suggest a near kinematical distance of about 4.8 kpc. They also estimated the distance based on a Sedov solution (Sedov 1959; Hamilton et al. 1983) from the observed X-ray temperature and the angular radius to derive  $3.2 \text{ kpc} \leq d \leq 4.3 \text{ kpc}$  for an assumed initial energy of  $10^{51}$  ergs. In this paper, we adopt  $d = 4.8$  kpc. They also estimated the age of the SNR, based on a Sedov solution from the X-ray observation, to be  $1.5\text{--}2.8 \times 10^4$  years under the assumption of an initial energy of  $10^{51}$  ergs, and  $2.7\text{--}3.9 \times 10^4$  years under the assumption of a distance of 6 kpc. Similarly, we estimated an age of  $2.2\text{--}3.1 \times 10^4$  years under the assumption of a distance of 4.8 kpc. Odegard (1986) represented an age of  $1.5 \times 10^4$  years from the relation between the age and the surface brightness in the radio band.

PSR B1800–21: The young Vela-like pulsar B1800–21 was found in a radio observation (Clifton & Lyne 1986). The offset from the centroid of HESS J1804–216 is  $\sim 11$  arcmin. The spin period, the spin period derivative, and the characteristic age are  $P = 133.6$  ms,  $\dot{P} = 1.34 \times 10^{-13}$  s/s, and  $\tau_c = P/2\dot{P} = 15.8$  kyears, respectively (Briskin et al. 2006). The resulting spin-down luminosity is  $\dot{E} = 4\pi^2 I \dot{P}/P^3 = 2.2 \times 10^{36} (I/10^{45}) \text{ erg s}^{-1}$ , where  $I$  is the moment of inertia in units of  $\text{g cm}^2$ . The distance was estimated to be 3.9 kpc from the pulsar’s dispersion measure of  $233.99 \text{ pc cm}^{-3}$  (Tayler & Cordes 1993). The newer Cordes & Lazio NE2001 model (Cordes & Lazio 2002) gives a similar distance of  $3.84^{+0.39}_{-0.45}$  kpc. We adopt  $d = 3.84$  kpc throughout this paper. The association between PSR B1800–21 and G8.7–0.1 has been discussed in several papers (e.g. Finley & Ögelman 1994; Frail et al. 1994; Kassim & Weiler 1990a). However, a recent proper-motion measurement (Briskin et al. 2006) has shown that the pulsar was born outside the currently observed SNR, and that is moving more nearly toward the center of G8.7–0.1, rather than away from it, which makes their association very unlikely. Based on a 10 ks observation with the *ROSAT* PSPC, Finley & Ögelman (1994) reported a faint X-ray source near the radio pulsar position, and attributed this emission to PSR B1800–21. Recently, Kargaltsev et al. (2007a) and Cui & Konopelko (2006) reported that an X-ray nebula around the pulsar was detected with *Chandra*. Additionally, Kargaltsev et al. (2007a) reported that the X-ray

nebula has two structures: a brighter compact ( $\sim 7'' \times 4''$ ) component (the inner pulsar wind nebula (PWN)) and an extended ( $\sim 12''$ ) fainter emission component (the outer PWN). These are asymmetric to the pulsar position and extended toward HESS J1804–216.

SNR G8.31–0.09: SNR G8.31–0.09 was found in a 90 cm multi-configuration Very Large Array survey of the Galactic plane. The size is  $5' \times 4'$ , and the offset from the centroid of HESS J1804–216 is 7 arcmin. The morphology is shell-like and the spectral index is  $\alpha_r = -0.6$  for  $F_\nu \propto \nu^{\alpha_r}$  (Brogan et al. 2006).

Suzaku Src1: The offset from the centroid of HESS J1804–216 is 3 arcmin. Bamba et al. (2007) reported that Src1 is point-like or compact compared to the spatial resolution of *Suzaku* with a half-power diameter of about 2 arcmin. However, Kargaltsev et al. (2007b) reported that Src1 is extended or multiple ( $1.5' - 2'$ ) with a *Chandra* observation. The *Suzaku* spectrum was fitted with an absorbed power-law model (Bamba et al. 2007). The best-fit absorbing column is consistent with the Galactic hydrogen column in that direction. Since the photon index of  $-0.3 \pm 0.5$  is very flat, Bamba et al. (2007) suggest that this source is likely to be a high-mass X-ray binary (HMXB). In the *Chandra* observation (Kargaltsev et al. 2007b), no spectral fitting was able to be performed because of the low signal-to-noise ratio. The unabsorbed flux, which was estimated from the *Chandra* observation using the best-fit parameters reported by Bamba et al. (2007), is a factor of  $\approx 1.7$  smaller than that reported with the *Suzaku* observation of Bamba et al. (2007). The difference could be due to unaccounted systematic errors, or the variability of the source, which supports the HMXB interpretation (Kargaltsev et al. 2007b).

Suzaku Src2: The offset from the centroid of HESS J1804–216 is 1.8 arcmin. Though Bamba et al. (2007) reported that Src2 is extended or multiple, based on the *Suzaku* observation, Kargaltsev et al. (2007b) reported that Src2 is point-like in a *Chandra* observation. This could mean that the more sensitive *Suzaku* observations have detected a fainter extended PWN component. The *Suzaku* spectrum was fitted with an absorbed power-law model (Bamba et al. 2007), and the best-fit absorbing column is about an order-of-magnitude higher than the expected Galactic column. This implies that Src2 is embedded in dense gas. The *Chandra* spectrum was also well-fitted with an absorbed power-law model, and the obtained absorbing column density is a factor of 2–3 larger than the Galactic column (Kargaltsev et al. 2007b). Kargaltsev et al. (2007b) stated that the large absorption suggests that Src2 is located within (or even beyond) the Galactic Bulge, or it shows an intrinsic absorption, which is often seen in the X-ray spectra of HMXBs. Kargaltsev et al. (2007b) also reported a marginal pulsation of 106 s in Src2, which supports an HMXB interpretation. On the other hand, Bamba et al. (2007) suggested that Src2 is a PWN or a shell-like SNR because of the extended morphology observed with *Suzaku* and the best-fit photon index of 1.7 (0.7–3.1).

None of the above five sources morphologically match HESS J1804–216. The counterpart is therefore still unknown. In this paper, we present TeV gamma-ray observations of HESS J1804–216 with the CANGAROO-III telescopes and discuss the radiation mechanism and the counterpart by combining our result with multi-

wavelength observations.

## 2. CANGAROO-III OBSERVATIONS

CANGAROO-III is an array of four IACTs, located near Woomera, South Australia (136°47'E, 31°06'S, 160 m a.s.l.). Each telescope has a 10 m diameter reflector made up of 114 segmented FRP spherical mirrors mounted on a parabolic frame (Kawachi et al. 2001). The telescopes are situated at the corners of a diamond with sides of  $\sim 100$  m (Enomoto et al. 2002). The oldest telescope, T1, which was the CANGAROO-II telescope, was not used due to its smaller FOV and higher energy threshold. The imaging camera systems on the other three telescopes (T2, T3 and T4) are identical, with 427 PMTs and a FOV of  $4.0^\circ$  (Kabuki et al. 2003). The PMT signals were recorded by charge ADCs and multi-hit TDCs (Kubo et al. 2001). The observations of HESS J1804–216 were made from May to July, 2006, using the ‘wobble’ mode in which the pointing position of each telescope was shifted in declination by  $\pm 0.5^\circ$  from the centroid of HESS J1804–216. The mean zenith angle of the observation was  $21^\circ$ , and the total observation time was 86.8 hr. We used the 3-fold coincidence data taken at zenith angles of less than  $40^\circ$ . To trigger data recording, an individual telescope was required to have more than four pixels receiving over 7.6 photoelectrons within 100 ns (local trigger), with a global trigger system to determine the coincidence of any two of the three telescopes (Nishijima et al. 2005). We rejected data taken under bad weather conditions in which the shower event rate was less than 6 Hz. Taking into account the DAQ dead-time, the effective live time was calculated to be 76 hr.

## 3. DATA REDUCTION AND ANALYSIS

The basic analysis procedures are described in detail in Enomoto et al. (2006a) and Kabuki et al. (2007). Using calibration data taken daily with LEDs, the recorded charges of each pixel in the camera were converted to the number of photoelectrons. At this step we found 7 bad pixels out of 427 pixels for T2, 5 for T3, and 1 for T4, due to their higher or lower ADC conversion factors in these observations. These bad pixels were removed from this analysis, which was also reflected in the Monte Carlo simulations. After that, every shower image was cleaned through the following CANGAROO-III standard criteria. Only pixels that received  $\geq 5.0$  photoelectrons were used as “hit pixels”. Then, five or more adjacent hit pixels, with arrival times of within 30 ns from the average hit time of all pixels, were recognized as a shower cluster.

Before calculating image moments — the “Hillas parameters” (Hillas 1985) — we applied the “edge cut” described in Enomoto et al. (2006b). We rejected events with any hits in the outer-most layer of the camera. The orientation angles were determined by minimizing the sum of the squared widths with a constraint given by the distance predicted by Monte Carlo simulations.

We then applied the Fisher Discriminant method (Fisher 1936; Enomoto et al. 2006a) with a multi-parameter set of  $\vec{P} = (W_2, W_3, W_4, L_2, L_3, L_4)$ , where  $W$  and  $L$  are the energy corrected width and length, and the suffixes represent the telescope IDs. The Fisher Discriminant (FD) is defined as  $FD \equiv \vec{\alpha} \cdot \vec{P}$ , where  $\vec{\alpha}$  is a set of coefficients mathematically determined in order

to maximize the separation between two FDs for gamma rays and hadrons.

For a background study we selected a ring region around the target,  $0.3 \leq \theta^2 \leq 0.5 \text{ deg}^2$ , where  $\theta$  is the angular distance to the centroid of HESS J1804–216 reported by the H.E.S.S. group (Aharonian et al. 2006a), and obtained the FD distributions for the background,  $F_b$ , and Monte Carlo gamma rays,  $F_g$ . Finally, we could fit the FD distributions of the events from the target with a linear combination of these two components. The observed FD distributions,  $F$ , should be represented as  $F = \alpha F_g + (1 - \alpha) F_b$ , where  $\alpha$  is the ratio of gamma-ray events to the total number of events. Here, only  $\alpha$  was optimized. This analysis method was verified by an analysis of the Crab nebula data taken in December, 2005.

The reflectivities of each telescope, which were used in the Monte Carlo simulations, were monitored every month by a muon ring analysis of a calibration run taken individually by each telescope. We obtained relative light-collecting efficiencies with respect to the original mirror production times of 0.60, 0.60 and 0.65 for T2, T3 and T4, respectively. Throughout this analysis, we used the Monte Carlo simulations for gamma rays assuming a point-source.

## 4. RESULTS

The obtained  $\theta^2$  plot is shown in Fig. 1 with the point spread function (PSF) of our telescopes,  $0.23^\circ$  (68% containment radius). The numbers of excess events that we detected above 600 GeV were  $512 \pm 61$  within  $\theta^2 < 0.06 \text{ deg}^2$ , based on the assumption that it was a point source,  $977 \pm 94$  within  $\theta^2 < 0.17 \text{ deg}^2$ , which corresponds to that used in the spectral analysis by H.E.S.S. (and taking into account the difference between our PSF and that of H.E.S.S.), and  $1389 \pm 126$  within  $\theta^2 < 0.3 \text{ deg}^2$ . The TeV gamma-ray emission is extended, and the morphology of gamma-ray-like events, derived with boxcar smoothing with each pixel replaced by the average of its square neighborhood, is shown in Fig. 2. The number of excess events was individually estimated by the FD-fitting method in each  $0.2^\circ \times 0.2^\circ$  sky bin. When we evaluated the outer regions ( $\theta^2 > 0.6 \text{ deg}^2$ ), we had to consider gradual deformations of the FD distributions at larger angular distances from the target. Therefore, we selected an annulus with radii  $0.2^\circ < r < 0.4^\circ$  centered on the evaluated region as the background. For the inner regions,  $\theta^2 < 0.6 \text{ deg}^2$ , the events in  $0.3 \leq \theta^2 \leq 0.5 \text{ deg}^2$ , excluding the evaluated region, were adopted as a background. The intrinsic extent of the TeV gamma-ray emission was estimated by a 2D Gaussian fit on our unsmoothed excess map. The intrinsic deviations along the Right Ascension and Declination axes were calculated to be  $0.160^\circ \pm 0.005^\circ$  and  $0.274^\circ \pm 0.011^\circ$ , respectively. The best-fit centroid position was obtained (R.A., dec [J2000]) =  $(271.079^\circ, -21.727^\circ)$ . The offset from the best-fit position reported by H.E.S.S. (Aharonian et al. 2006a) is  $(\Delta \text{R.A.}, \Delta \text{dec}) = (-0.053^\circ \pm 0.007^\circ, -0.026^\circ \pm 0.013^\circ)$ . The offset is not significant given our PSF.

Figure 3 represents a reconstructed VHE gamma-ray differential spectrum compatible with a single power-law:  $(5.0 \pm 1.5_{\text{stat}} \pm 1.6_{\text{sys}}) \times 10^{-12} (\text{E}/1 \text{ TeV})^{-\alpha} \text{ cm}^{-2} \text{ s}^{-1} \text{ TeV}^{-1}$  with a photon index  $\alpha$  of  $2.69 \pm 0.30_{\text{stat}} \pm 0.34_{\text{sys}}$ . To obtain the spectrum, we used a cut of  $\theta^2 < 0.17 \text{ deg}^2$ . The relevant systematic errors are due to

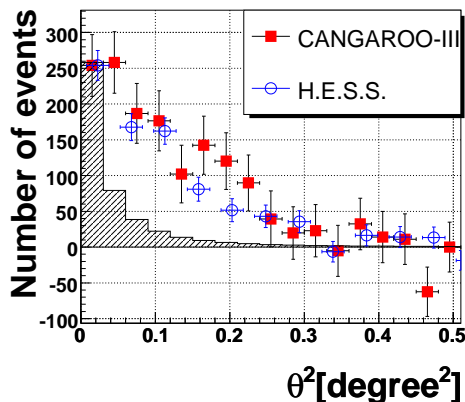


FIG. 1.— Number of excess events as a function of the squared angular distance. Here,  $0^\circ$  corresponds to the centroid of HESS J1804–216 reported by the H.E.S.S. group (Aharonian et al. 2006a). The squares show the CANGAROO-III data points. The circles show the normalized H.E.S.S. data points. The hatched histogram represents our PSF for a comparison.

the atmospheric transparency, night sky background fluctuations, uniformity of camera pixels, and light-collecting efficiencies. In addition, the signal integrating region was changed from  $\theta^2 \leq 0.17 \text{ deg}^2$  to  $0.3 \text{ deg}^2$ , and the difference in fluxes was incorporated in the systematic errors. The TeV gamma-ray extension and the flux obtained by CANGAROO-III were consistent with those by H.E.S.S. Our result indicates that the TeV gamma-ray emission was unchanged between the H.E.S.S. observations in 2004 and ours in 2006.

## 5. DISCUSSION

As described in §1, there are 5 possible counterparts: SNR G8.7–0.1, PSR B1800–21, SNR G8.31–0.09, Suzaku Src1, and Suzaku Src2. Figures 4 and 5 show the spectral energy distribution (SED) of these counterparts and HESS J1804–216 including the results of this work. We extend the introductions to these sources given in §1 with a more detailed summary of the sources and their characteristics in the following paragraphs.

Bamba et al. (2007) state that Suzaku Src1 and Src2 are physically associated with HESS J1804–216. They suggested that X-rays and TeV gamma-ray emission could come from an SNR shock, based on a model proposed by Yamazaki et al. (2006); in an old SNR with an age of  $\sim 10^5$  years, primary electrons have already lost most of their energy, and only nucleonic cosmic rays remain. Additionally, the old SNR shock colliding with a giant molecular cloud (GMC) can emit hard nonthermal X-rays from secondary electrons and strong TeV gamma rays from shock accelerated protons through  $\pi^0$  decay. This model can explain the observed large ratio of the TeV gamma-ray to X-ray flux (factors of  $\sim 100$ ). The large X-ray absorption of Src2 also supports this scenario.

Kargaltsev et al. (2007b) suggested that a PWN is the source of HESS J1804–216, like HESS J1825–137 or Vela X. HESS J1825–137 is likely to be associated with the PWN G18.0–0.7 around the Vela-like pulsar B1823–13. The TeV gamma-ray emission detected with

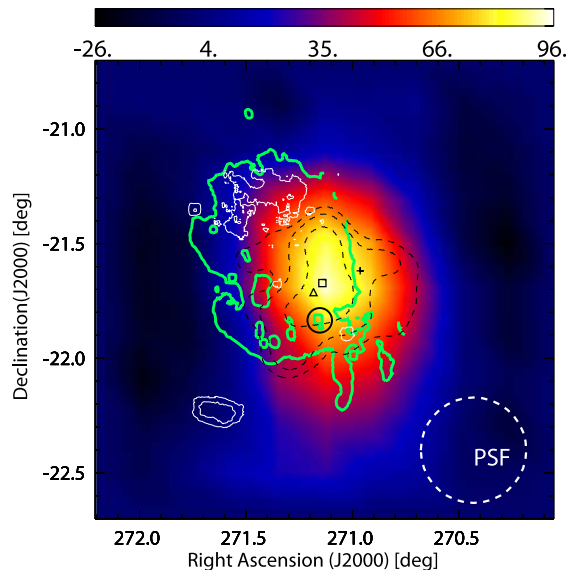


FIG. 2.— Smoothed morphology of gamma-ray-like events with our PSF of  $0.23^\circ$  radius. Dashed contours show the VHE gamma-ray emission seen by H.E.S.S. (Aharonian et al. 2006a). The thick solid contours (green) show the 20 cm radio emission from G8.7–0.1 recorded by the VLA (White et al. 2005). The thin solid contours (white) show the X-ray emission detected by the *ROSAT* satellite (Finley & Ögelman 1994). The solid circle indicates the position of G8.31–0.09 (Brogan et al. 2006). The cross indicates the PSR B1800–21 position (Briskin et al. 2006). The triangle and the square indicate the position of Suzaku Src1 and Suzaku Src2, respectively.

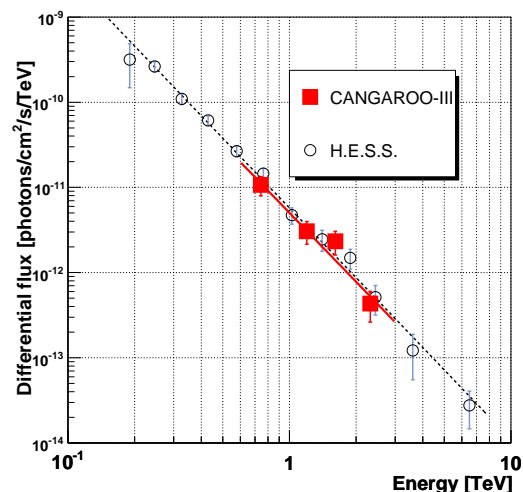


FIG. 3.— Differential flux. The squares and circles show the CANGAROO-III and the H.E.S.S. data points, respectively. The best-fit power-law is also shown by the solid and dashed line from this work and from H.E.S.S., respectively.

H.E.S.S. covers a much larger area than the X-ray emission from G18.0–0.7, extending up to  $1^\circ$  southward from the pulsar (Aharonian et al. 2005b). However, both the TeV gamma-ray and the low surface-brightness X-ray emission have similarly asymmetric shapes, and they are offset in the same direction with respect to the pulsar position. A similar picture is observed around the Vela pulsar (Aharonian et al. 2006b). These phenomena can be explained by the “crushed PWN” hypothesis (Blondin et al. 2001): on a time scale of  $\sim 10^4$  years, the reverse SNR shock front propagates toward the center of

the remnant, where it crushes the PWN, and asymmetries in the surrounding interstellar medium give rise to an asymmetric shape and offset of the PWN relative to the pulsar and explosion site.

Kargaltsev et al. (2007b) considered the possibility that Suzaku Src1 or Src2 are a PWN powering HESS J1804–216. However, the 3.24 s time resolution of the *Chandra* ACIS observation precludes a search for the subsecond pulse periods expected for a young pulsar. Therefore, there is no strong evidence to support it at this point. They also suggested that PSR B1800–21 is associated with HESS J1804–216. Its asymmetric PWN component extending toward HESS J1804–216, detected by *Chandra* (Kargaltsev et al. 2007a), shows a hint of the association, but the sensitivity of the *Chandra* observation was possibly insufficient to detect the PWN beyond 15''–20'' from the pulsar. Additionally, they pointed out that the extended morphology of HESS J1804–216 argues against the HMXB interpretation because of the weak observational evidence for HMXBs producing extended TeV gamma-ray emission.

Fatuzzo et al. (2006) concluded that PSR B1800–21 cannot account for the spectrum of HESS J1804–216, and G8.7–0.1 is probably the source of the TeV gamma rays. However, they considered only a pion-decay model without any consideration of the inverse Compton process, and for PSR B1800–21 they only considered the acceleration of charged particles across voltage drops in the relativistic winds near the light cylinder. Additionally, they did not take into account the possibility of other sources besides PSR B1800–21 and G8.7–0.1.

Based on the above discussions and the SED, we now discuss the radiation mechanism of HESS J1804–216 and its counterpart. For Suzaku Src1, Bamba et al. (2007) reported a very hard photon index of  $-0.3 \pm 0.5$ , which corresponds to the power-law index of electrons of  $-1.6 \pm 1.0$ . This unusual value indicates that the X-ray emission is not synchrotron radiation. Therefore, we do not discuss the SED of Src1. Bamba et al. (2007) suggested that Src1 might be an HMXB. If it were, the association between Src1 and HESS J1804–216 would be unlikely as discussed in Kargaltsev et al. (2007b). The results of independent observations of the H.E.S.S. and CANGAROO-III telescopes show that HESS J1804–216 is quite extended ( $\sim 0.4^\circ$ ). This precludes the possibility that HESS J1804–216 is an Active Galactic Nucleus. The plausible candidates seem to be an SNR or a PWN.

### 5.1. SNR origin

The SNR candidates associated with HESS J1804–216 are SNR G8.7–0.1, SNR G8.31–0.09, and Suzaku Src2.

**SNR G8.7–0.1:** We discuss the association between HESS J1804–216 and SNR G8.7–0.1. Figure 6 shows the leptonic model curves used to fit the TeV gamma-ray spectra obtained by H.E.S.S. and CANGAROO-III. We examined plausible inverse Compton (IC) model curves on the assumption that the electron spectrum is a single power-law with an exponential cutoff,

$$\frac{dN_e}{dE_e} = K_e E_e^{-\Gamma_e} \exp(-E_e/E_{max,e}), \quad (1)$$

where  $K_e$  is the normalization factor,  $E_e$  is the electron

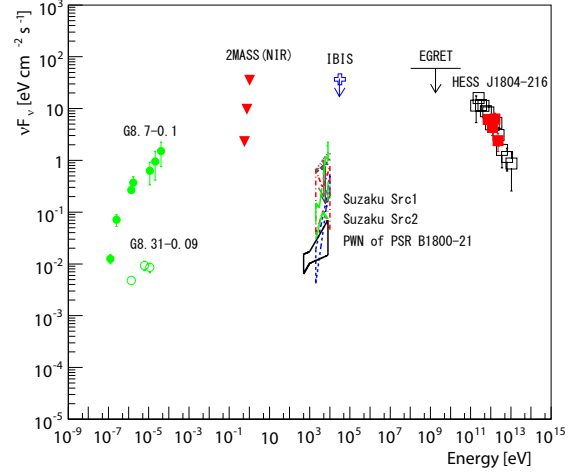


FIG. 4.— Spectral energy distribution (SED) of HESS J1804–216, SNR G8.7–0.1, SNR G8.31–0.09, PWN of PSR B1800–21, Suzaku Src1, and Suzaku Src2 in all energy bands. The data points derived from this work are represented by filled squares and references to others are given in Table 1.

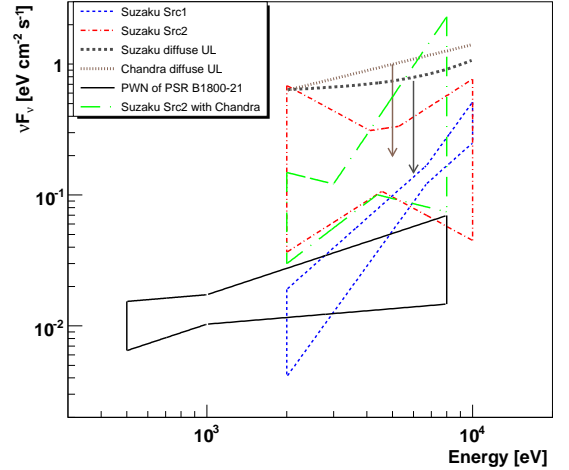


FIG. 5.— SED in the X-ray band. The dashed and dotted arrows show the upper limits for the diffuse source obtained by *Suzaku* and *Chandra*, respectively. The dashed, dot-and-short-dashed, dot-and-long-dashed, and solid closed regions show the error regions of Suzaku Src1, Suzaku Src2 with *Suzaku* telescope, Suzaku Src2 with *Chandra* telescope, and PWN of PSR B1800–21 with *Chandra* telescope, respectively.

energy,  $\Gamma_e$  is the spectral index of the injected electrons, and  $E_{max,e}$  is the maximum electron energy. In this paper, we do not consider hard spectra of electrons with  $\Gamma_e < 1$ .

To obtain the entire IC model curve, we used IR and optical (starlight) photon fields for the target photons in addition to the cosmic microwave background (CMB) field density. Here, we used an interstellar radiation field (ISRF) derived from the latest (v50p) GALPROP package (Porter & Strong 2005; Strong & Moskalenko 2006). The ISRF was given for three components (CMB, IR from dust, and optical starlight) as a function of the distance from the Galactic center,  $R$  (in kpc), and the distance from the Galactic plane,  $z$  (in kpc). We extracted the spectra at  $(R, z) = (3.8, -0.01)$  at the SNR G8.7–0.1 position, as shown in Fig. 7. The X-ray upper limits for diffuse emission constrained  $\Gamma_e$  to be less than 2.5 for the IC model curves. We obtained  $E_{max,e}$  to fit

the IC model curves to the TeV gamma-ray spectra for each fixed spectral index  $\Gamma_e$  (Table 2).

The electrons causing the IC scattering also emit synchrotron radiation. In the radio band, the spectrum of the whole region of G8.7–0.1 is regarded as the upper limits. Here, the upper limits in the near-infrared (NIR) band, in Fig. 4, are neglected because they are for point sources. The magnetic field is constrained by the radio upper limits and the X-ray upper limits for diffuse emission. Table 2 lists the upper limits of the magnetic field, maximum electron energy, and the total energy of electrons above 0.51 MeV,

$$W_e = \int_{0.51 \text{ MeV}}^{\infty} E_e \frac{dN_e}{dE_e} dE_e, \quad (2)$$

at  $d = 4.8$  kpc for each electron spectral index  $\Gamma_e$ .  $W_e$  is estimated to be less than  $\sim 10^{50}$  ergs for  $\Gamma_e \leq 2.5$ . Although the total explosion energy of some supernovae are much higher, for example, the total energy of SN2003lw, a type Ic supernova, is estimated to be  $\sim 6 \times 10^{52}$  ergs (Mazzali et al. 2006), the typical total energy of a supernova explosion is estimated to be  $\sim 10^{51}$  ergs. If the efficiency of the energy to accelerate the electrons is 10%, the obtained  $W_e$  can satisfy the SNR origin scenario.

Additionally, the hadronic scenario can also explain the TeV gamma-ray spectrum for G8.7–0.1. In Fig. 8, we show the  $\pi^0$  decay model curves with the assumption that the proton spectrum is a single power-law with an exponential cutoff,

$$\frac{dN_p}{dE_p} = K_p E_p^{-\Gamma_p} \exp(-E_p/E_{\text{max},p}), \quad (3)$$

where  $K_p$  is the normalization factor,  $E_p$  is the proton energy,  $\Gamma_p$  is the spectral index of the injected protons, and  $E_{\text{max},p}$  is the maximum proton energy. In this paper, we do not consider hard proton spectra with  $\Gamma_p < 1$ . The EGRET upper limit (Kargaltsev et al. 2007b; Hartman et al. 1999) constrained  $\Gamma_p$  to be less than 2.3. We obtained  $E_{\text{max},p}$  to fit the  $\pi^0$  decay model curves to the TeV gamma-ray spectra for each fixed spectral index  $\Gamma_p$ . Table 3 lists the fitting parameters and the total energy of protons above 1 GeV,

$$W_p = \int_{1 \text{ GeV}}^{\infty} E_p \frac{dN_p}{dE_p} dE_p, \quad (4)$$

at a distance for SNR G8.7–0.1 of 4.8 kpc with the assumption that the interstellar medium (ISM) density is  $n = 1 \text{ cm}^{-3}$ .

The total energy of protons,  $W_p$ , is  $9.3 \times 10^{51} (d/4.8 \text{ kpc})^2 (n/1 \text{ cm}^{-3})^{-1}$  ergs with  $\Gamma_p = 2.3$ . For a typical total supernova explosion energy of  $\sim 10^{51}$  ergs, if the efficiency of the energy to accelerate the protons is 10%, the ISM density should be  $n \sim 10^2 \text{ cm}^{-3}$ . With the assumption of  $\Gamma_p = 1.0$ ,  $W_p$  is  $9.6 \times 10^{50} (d/4.8 \text{ kpc})^2 (n/1 \text{ cm}^{-3})^{-1}$  ergs, and the ISM density should be  $n \sim 10 \text{ cm}^{-3}$  for an efficiency of 10%. However, Finley & Ögelman (1994) derived the electron density  $n_e$  to be  $(0.1 - 0.2)(d/6 \text{ kpc})^{-1/2} \text{ cm}^{-3}$  for an X-ray emitting gas in the remnant, based on the *ROSAT* observation. In addition, the lack of the X-ray emission in the TeV gamma-ray emission region, shown in Fig. 2, indicates that the ambient density at the region

is lower than that at the X-ray emitting region, that is,  $n < 0.1 - 0.2 \text{ cm}^{-3}$ . If it were, the hadronic scenario would be unlikely. On the other hand, a GMC, SRBY3, is near (in projection) to HESS J1804–216. The offset, the angular radius, the distance, and the mass of the cloud are  $\sim 0.1^\circ$ ,  $\sim 0.2^\circ$ , 5.3 kpc,  $55.6 \times 10^4 M_\odot$ , respectively (Cramphorn & Sunyaev 2002). The mean number density is calculated to be  $\sim 4.5 \times 10^2 \text{ cm}^{-3}$  under the assumption that it is spherical symmetry. If it is associated with HESS J1804–216, there can be a high-density medium, and the hadronic scenario can be satisfied.

Additionally, we estimated  $K_{pe}$ , the number ratio of protons to primary electrons. Under the assumption that the spectral indices of the protons and primary electrons are the same,  $\Gamma_p = \Gamma_e$ ,  $K_{pe}$  is derived from eqs.(1)(3) as  $K_{pe} = K_p/K_e$ . Generally the maximum electron energy  $E_{\text{max},e}$  is the same as  $E_{\text{max},p}$ , or  $E_{\text{max},e}$  is lower than  $E_{\text{max},p}$  due to a cooling effect, that is,  $E_{\text{max},e} \leq E_{\text{max},p}$ . In Fig. 8, we show the leptonic model curves with the assumption of  $K_{pe} \sim 10^5 (n/1 \text{ cm}^{-3})^{-1}$ ,  $B = 3 \mu\text{G}$ ,  $\Gamma_e = 2.0$ , and  $E_{\text{max},e} = E_{\text{max},p} = 16 \text{ TeV}$ . The leptonic model curves move up with the lower  $K_{pe}$ . With the assumption of  $B = 3 \mu\text{G}$ ,  $K_{pe}$  is constrained to be  $K_{pe} \geq 10^4 (n/1 \text{ cm}^{-3})^{-1}$ , because the IC model curve cannot exceed the TeV gamma-ray spectrum. If a GMC is associated with HESS J1804–216, and  $n \sim 10^2 \text{ cm}^{-3}$ , the obtained  $K_{pe}$  is consistent with that of the average cosmic rays in our Galaxy,  $K_{pe} \sim 10^2$ . On the other hand, for a high  $K_{pe}n$  of  $\sim 10^4$ , we need to consider the contribution of the emission from secondary electrons produced by charged pions (Yamazaki et al. 2006; Pfrommer & Enßlin 2004). However, a detailed discussion about secondary electrons is beyond the scope of this paper.

**Suzaku Src2:** For Suzaku Src2, we used the overlapping error region obtained by *Suzaku* and *Chandra*. In Fig. 9, we examined plausible synchrotron model curve within the error of the unabsorbed X-ray flux on the same assumption as eq. (1) with adopting  $B=3 \mu\text{G}$  and  $\Gamma_e = 2.0$ . The obtained IC model curves for the same electron spectrum cannot reproduce the TeV gamma-ray spectrum. Even if the higher IR energy density than that in GALPROP is adopted, the cutoff energy of the models does not change from  $\sim 10 \text{ TeV}$ , while the observed cutoff energy should be  $\leq 0.3 \text{ TeV}$ ; such a low cutoff energy is due to the soft spectrum of HESS J1804–216. A stronger magnetic field can reduce the cutoff energy of the IC model curves. In order to make the cutoff energy of 0.3 TeV for Suzaku Src2, the magnetic field should be more than 7 mG, and to fit the TeV gamma-ray spectrum with the magnetic field the IR energy density should be  $\sim 10^6$  times higher than that in GALPROP. These values are unlikely. We therefore conclude that the TeV gamma-ray spectra are not produced by the IC model curves for the electron spectrum.

We also examined the bremsstrahlung emission for the same electron spectrum. To fit the TeV gamma-ray spectrum, the ISM density should be more than  $\sim 10^8 \text{ cm}^{-3}$ , and the magnetic field should be stronger than 1.8 mG for Suzaku Src2. Due to such incredibly high values of the ISM density and the magnetic field, we also reject the scenario that the bremsstrahlung radiation produces the TeV gamma-ray spectrum.



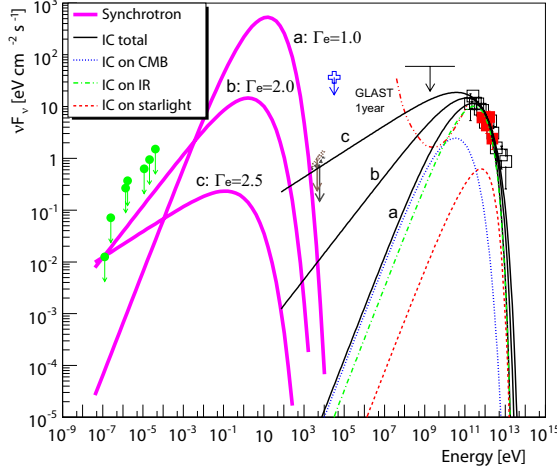


FIG. 6.— Leptonic scenario for SNR G8.7–0.1. The thick solid curves show the synchrotron emissions, and the thin solid curves show the total IC spectra with fixed spectral indices of  $\Gamma_e = 1.0$  (a),  $\Gamma_e = 2.0$  (b), and  $\Gamma_e = 2.5$  (c), and with  $B$  of  $50 \mu\text{G}$ ,  $8 \mu\text{G}$ ,  $3 \mu\text{G}$ , respectively. The dotted, dot-dashed, and dashed curves show the IC spectra (a) on each of CMB, IR and starlight, shown in Fig. 7, respectively. The dash-dot-dotted curve shows the 1 year,  $5\sigma$  sensitivity for the *GLAST* LAT taking into account the diffuse background at the position of HESS J1804–216 (*GLAST* LAT 2007).

A simple solution to explain the observed TeV gamma-ray spectrum is that accelerated protons produce the gamma rays, as shown in Fig. 9. Therefore, the TeV gamma rays and the X-rays could be produced by accelerated protons and electrons, respectively. Assuming the spectral index,  $\Gamma_p = \Gamma_e = 2.0$ , the maximum electron energy is  $E_{\text{max},e} \leq E_{\text{max},p} = 16 \text{ TeV}$  (Table 3), and this maximum energy makes the lower limit of the magnetic field of  $B \geq 130 \mu\text{G}$  to fit the X-ray data. With the magnetic field, we calculated the lower limit of  $K_{pe} \geq 6.6 \times 10^7 (n/1 \text{ cm}^{-3})^{-1}$ . This value is much higher than that of the average cosmic rays in our Galaxy,  $K_{pe} \sim 10^2$ .

**G8.31–0.09:** We consider the possibility that HESS J1804–216 is associated with G8.31–0.09. For the leptonic scenario, it is difficult to explain the fact that the size of G8.31–0.09 in the radio band is much smaller than that in the TeV emission region. On the other hand, if the accelerated protons produced the TeV gamma rays, the difference in the size could be explained due to the difference of the diffusion length between protons and primary electrons. However, we need additional information, either on the distance or from other wavelengths, to discuss the energetics or  $K_{pe}$ .

### 5.2. PWN origin

At the present time, PWNe are the largest population of identified TeV galactic sources, and the number of TeV gamma-ray sources that are located near a plausible pulsar candidate are increasing (Hinton 2007). Therefore, it is very important to consider the PWN origin. The PWN candidates associated with HESS J1804–216 are the PWN of PSR B1800–21, and Suzaku Src2.

**PWN of PSR B1800–21:** To estimate the total energy supplied from a pulsar, we should consider any braking effects for spin-down luminosity. If a pulsar spins down from an initial spin period of  $P_0$  according

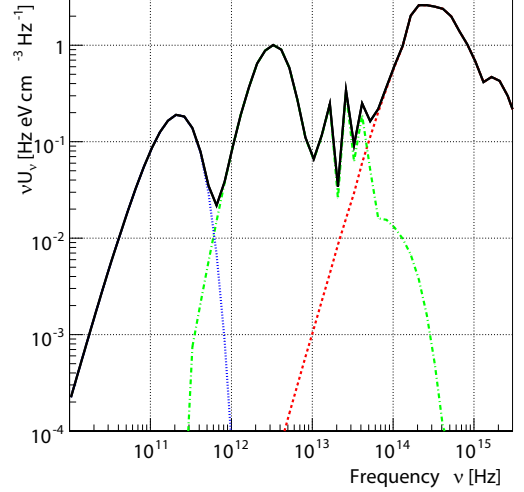


FIG. 7.— Interstellar radiation field from the GALPROP package (*v50p*) at  $(R, z) = (3.8, -0.01) \text{ kpc}$  for G8.7–0.1. From lower frequencies, CMB (dotted), IR emission from interstellar dust (dot-dashed), and optical photons from stars (dashed) are shown. The solid line represents the sum of the three components.

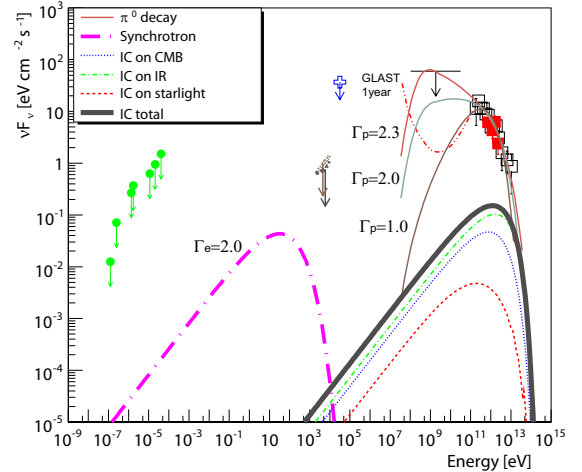


FIG. 8.— Hadronic scenario for SNR G8.7–0.1. The thin solid curves show the  $\pi^0$  decay model curves with fixed spectral indices of  $\Gamma_p = 2.3$ ,  $\Gamma_p = 2.0$ , and  $\Gamma_p = 1.0$ , respectively. The thick solid curve shows the total IC spectra, and the dot-and-long dashed curve shows the synchrotron emissions from the primary electrons with the assumption of  $\Gamma_e = 2.0$ ,  $B = 3 \mu\text{G}$ , and  $K_{pe} = 10^5 (n/1 \text{ cm}^{-3})^{-1}$ . The dotted, dot-dashed, and dashed curves show the IC spectra on each of CMB, IR and starlight, shown in Fig. 7, respectively.

to  $\dot{\Omega} = -k\Omega^{n_{br}}$  assuming both  $n_{br}$  and  $k$  are constant, where  $n_{br}$  is the braking index of the pulsar, the spin-down luminosity,  $\dot{E}(t)$ , is given as

$$\dot{E}(t) = \dot{E}_0 \left(1 + \frac{t}{\tau_0}\right)^{-\alpha}, \quad \alpha = \frac{n_{br} + 1}{n_{br} - 1}, \quad (5)$$

$$\tau_0 \equiv \frac{P_0}{(n_{br} - 1)\dot{P}_0} = \frac{P(t)}{(n_{br} - 1)\dot{P}(t)} - t, \quad (6)$$

where  $\tau_0$  is the initial spin-down timescale (Pacini & Salvati 1973). Therefore, the total energy that the pulsar has lost over its age,  $\tau$ , is

$$E_{\text{pwn}} = \int_0^\tau \dot{E}(t) dt = \frac{\dot{E}_0 \tau_0}{1 - \alpha} \left[ \left(1 + \frac{\tau}{\tau_0}\right)^{1-\alpha} - 1 \right]. \quad (7)$$

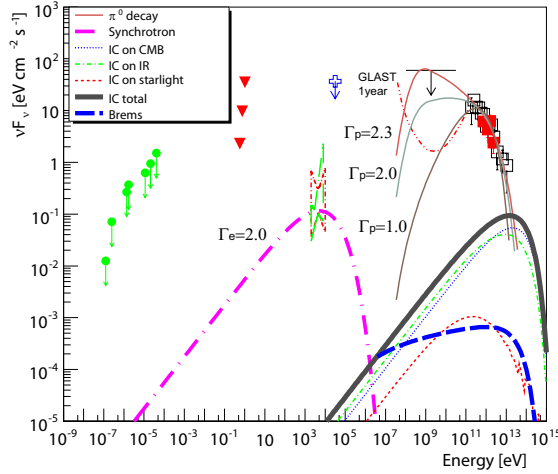


FIG. 9.— SED with leptonic model curves to fit Suzaku Src2 and  $\pi^0$  decay model curves to fit TeV gamma rays. The thick solid curve shows the total IC spectra, and the dot-and-long dashed curve shows the synchrotron emissions to fit Src2 with the assumption of a spectral index of  $\Gamma_e = 2.0$  and  $B = 3 \mu\text{G}$ . The dotted, dot-dashed, and dashed curves show the IC spectra on each of CMB, IR and starlight, shown in Fig. 7, respectively. The long dashed curve shows the bremsstrahlung for the same electron spectrum with the assumption of  $n = 1.0 \text{ cm}^{-3}$ . The thin solid curves show the  $\pi^0$  decay model curves with fixed spectral indices of  $\Gamma_p = 2.3$ ,  $\Gamma_p = 2.0$ , and  $\Gamma_p = 1.0$ , respectively.

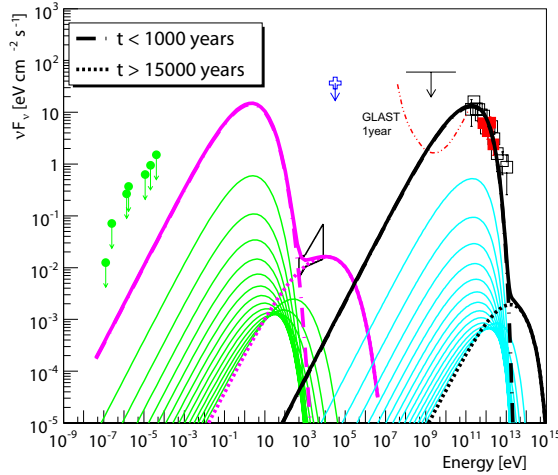


FIG. 10.— SED and the leptonic model curves for the PWN of PSR B1800–21 with a time-dependent rate of electrons-injection with  $\tau = 16$  kyears,  $\tau_0 = 700$  years, a braking index of  $n_{br} \sim 1.6$ ,  $\Gamma_e = 1.5$ , and  $B = 8 \mu\text{G}$ . The right-hand curves show the IC component, and the left-hand curves show the synchrotron emissions. The dot-dashed curves show the spectra produced by old electrons ( $t < 1000$  years), and the dotted curves show the spectra produced by young electrons ( $t > 15000$  years). The thin solid curves represent their medium per 1000 years ( $1000 < t < 15000$  years), and the thick solid curves show their total.

For the Crab pulsar, produced in the supernova of 1054, a  $\tau_0$  of  $\sim 700$  years is derived from eq. (6), and the total energy is derived as  $E_{\text{pwn}} = 3.8 \times 10^{49}$  ergs with a braking index of  $n_{br} = 2.5$  from eq. (7) (Livingstone et al. 2006). For PSR B1800–21, the braking index and the true age are unknown. The measured braking indices of other pulsars fall in the range of  $1.4 \leq n_{br} < 3$  (Livingstone et al. 2006). Therefore, we estimated the total energies for several braking indices with  $\dot{E}(\tau) = 2.2 \times 10^{36}$  ergs/s, an age of  $\tau = 15.8$  kyears (the same value as the characteristic age), and  $\tau_0 = 700$  years (the same as the Crab pulsar),

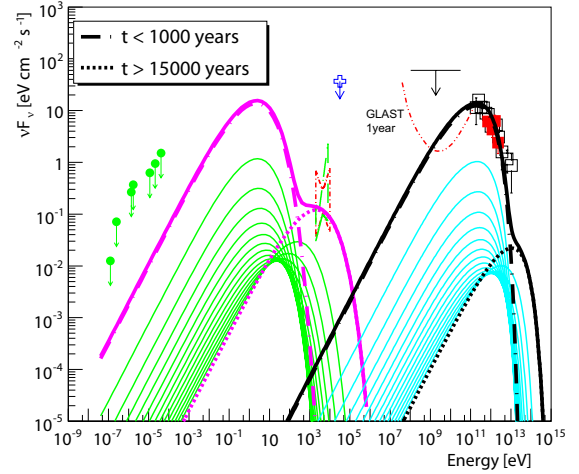


FIG. 11.— SED and the leptonic model curves for Suzaku Src2 with a time-dependent rate of electrons-injection with  $\tau = 16$  kyears,  $\tau_0 = 700$  years, a braking index of  $n_{br} \sim 1.8$ ,  $\Gamma_e = 1.5$ , and  $B = 8 \mu\text{G}$ . The model curves are the same as in Fig. 10.

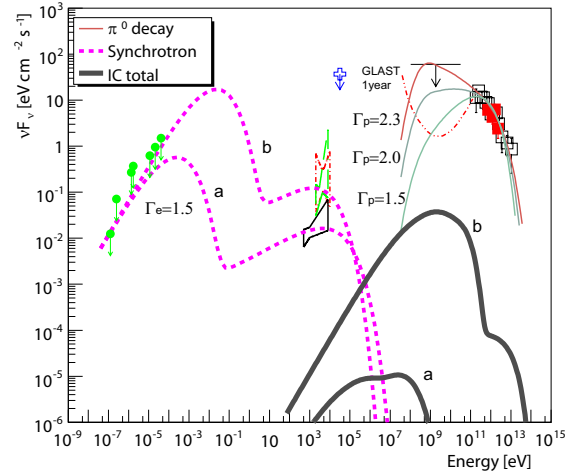


FIG. 12.— Hadronic scenario for PWN of PSR B1800–21 (a) and Suzaku Src2 (b). The thin solid curves show the  $\pi^0$  decay model curves with fixed spectral indices of  $\Gamma_p = 2.3$ ,  $\Gamma_p = 2.0$ , and  $\Gamma_p = 1.5$ , respectively. The thick solid curves show the total IC spectra, and the dashed curves show the total synchrotron emissions from primary electrons with  $\tau = 16$  kyears,  $\tau_0 = 700$  years, a braking index of  $n_{br} \sim 1.6$ ,  $\Gamma_e = 1.5$ ,  $B = 4 \text{ mG}$  for PWN of PSR B1800–21 (a), and  $B = 600 \mu\text{G}$  for Src2 (b).

which are listed in Table 4.

For the leptonic model, we assumed that the rate of electrons-injection,  $K'_e(t)$ , proportionally decreases with  $\dot{E}(t)$ , that is,  $K'_e(t) \propto \dot{E}(t)$ , and we considered the cooling effect due to synchrotron and IC energy losses (Funk et al. 2007). The old electrons that were injected with high-power initial spin-down luminosity have been cooled. On the other hand the young electrons have less time to be cooled. Figure 10 shows the SED with the leptonic model curves with a time-dependent rate of electrons-injection with  $\tau_0 = 700$  years, a braking index of  $n_{br} \sim 1.6$ , an age of  $\tau = 16$  kyears,  $\Gamma_e = 1.5$ , and  $B = 8 \mu\text{G}$ : To obtain the model curves, we used the broken energy due to synchrotron cooling and IC cooling,  $E_{br}(t) \sim 3m_e^2 c^3 / (4\sigma_T(\tau - t)(B^2/(8\pi) + W_{ph}))$ , where  $\sigma_T$  is the Thomson cross-section and  $W_{ph}$  is the total energy density of the photon field. For the PWN of PSR B1800–21, we used the error region for the entire PWN



(inner + outer) obtained by *Chandra* (Kargaltsev et al. 2007a). The old electrons are responsible for the TeV gamma-ray emission, and the young electrons are responsible for the X-ray emission. This picture may also explain the size difference between the TeV gamma-ray and the X-ray emission regions, because the old electrons can extend further than the young ones. To calculate the total energy of electrons,  $W_e$ , for the PWN origin scenario, we substituted  $E_{br}(t)$  for  $E_{max,e}$ . Then,  $W_e$  is estimated to be  $\sim 1.7 \times 10^{48}$  ergs for the above parameters. An  $E_{pwn}$  of  $1.3 \times 10^{52}$  ergs for the same parameters can easily explain the amount of electron energy, and the efficiency of the energy to accelerate electrons is  $\sim 1.3 \times 10^{-2}\%$ . Note that the above parameters are not unique, and other combinations of a  $\tau_0$  and a braking index are possible. If we adopt  $\tau_0 = 30$  years, acceptable model curves can be derived with a braking index of  $n_{br} \sim 2.2$ , an age of  $\tau = 16$  kyears,  $\Gamma_e = 1.5$ , and  $B = 8 \mu\text{G}$ . For the latter parameters,  $E_{pwn}$  is estimated to be  $2.3 \times 10^{52}$  ergs, and  $W_e$  is  $\sim 1.7 \times 10^{48}$  ergs. The efficiency of the energy to accelerate the electrons is  $\sim 7.4 \times 10^{-3}\%$ . In either case, a quite high value for the total energy,  $E_{pwn}$ , that the pulsar has lost is required to explain the observed spectra.

We consider the hadronic model given in Fig. 12. Table 3 lists the fitting parameters and the total energy of protons  $W_p$  at a distance for PSR B1800–21 of 3.84 kpc with the assumption that the ISM density is  $n = 1 \text{ cm}^{-3}$ .  $W_p$  with  $\Gamma_p$  of 2.3 is estimated to be  $5.9 \times 10^{51} (d/3.84 \text{ kpc})^2 (n/1 \text{ cm}^{-3})^{-1}$  ergs. With a  $\Gamma_p$  of 1.0,  $W_p$  is estimated to be  $6.1 \times 10^{50} (d/3.84 \text{ kpc})^2 (n/1 \text{ cm}^{-3})^{-1}$  ergs. The magnetic field is constrained to be  $B \geq 4 \text{ mG}$  with the assumption of  $\Gamma_p = 1.5$  and the constraint of  $E_{max,e} \leq E_{max,p} = 7.9 \text{ TeV}$  (Table 3). The magnetic field is very high.  $K_{pe}$  is estimated to be more than  $1.6 \times 10^4 (n/1 \text{ cm}^{-3})^{-1}$ . If a GMC is associated with HESS J1804–216, and  $n \sim 10^2 \text{ cm}^{-3}$ , the obtained  $K_{pe}$  is consistent with that of the average cosmic rays in our Galaxy,  $K_{pe} \sim 10^2$ . However, the lower limit of the magnetic field is much higher than the typical interstellar magnetic field, and there is no evidence supporting such a high magnetic field in this position.

**Suzaku Src2:** For the leptonic model, a similar scenario as that for PWN of PSR B1800–21 can be considered for Suzaku Src2. However, because we have no information about the age and the spin-down luminosity of Suzaku Src2, we assume the same age and spin-down luminosity as that of PSR B1800–21. Figure 11 shows leptonic model curves for Suzaku Src2 with  $\tau_0 = 700$  years, a braking index of  $n_{br} \sim 1.8$ , an age of  $\tau = 16$  kyears,  $\Gamma_e = 1.5$ , and  $B = 8 \mu\text{G}$ . The total energy of the electrons is calculated to be  $W_e = 1.8 \times 10^{48} (d/3.84 \text{ kpc})^2$  ergs, and  $E_{pwn}$  is  $1.2 \times 10^{51}$  ergs. This  $E_{pwn}$  would be proportionally reduced if  $\dot{E}(\tau)$  is lower than that of PSR B1800–21. For example,  $E_{pwn}$  is estimated to be  $\sim 10^{50}$  ergs with the assumption of  $\dot{E}(\tau) \sim 10^{35} \text{ ergs s}^{-1}$ . Radio and X-ray observations with higher time resolutions might be able to detect a sub-second pulse period from this source, and further observations in the IR to UV band for a diffuse source in the extended region of HESS J1804–216 could contribute to a tighter solution

for the leptonic models.

We consider the hadronic model as given in Fig. 12. The magnetic field is constrained to be  $B \geq 600 \mu\text{G}$  with the assumption of  $\Gamma_p = 1.5$  and the constraint of  $E_{max,e} \leq E_{max,p} = 7.9 \text{ TeV}$  (Table 3).  $K_{pe}$  is estimated to be more than  $1.5 \times 10^3 (n/1 \text{ cm}^{-3})^{-1}$ . The lower limit of the magnetic field is much higher than the typical interstellar magnetic field.

## 6. CONCLUSIONS

CANGAROO-III observed HESS J1804–216, and detected gamma rays above 600 GeV at the  $10\sigma$  level during an effective exposure of 76 hr. The obtained differential flux is consistent with the previous H.E.S.S. result, and the obtained morphology shows extended emission compared to our Point Spread Function. We have discussed the radiation mechanism and considered the proposed counterparts to the TeV gamma-ray source. For the SNR scenario, the most plausible counterpart is the SNR G8.7–0.1, and both hadronic and leptonic processes can produce the observed TeV gamma-ray spectrum. We obtained upper limits of spectral indices,  $\Gamma_e \leq 2.5$  for leptonic scenario, and  $\Gamma_p \leq 2.3$  for hadronic scenario. The total energy of the primary electrons,  $W_e$ , is estimated to be  $3.3 \times 10^{50} (d/4.8 \text{ kpc})^2$  ergs with  $\Gamma_e = 2.5$ . The total energy of the protons,  $W_p$ , is estimated to be  $9.3 \times 10^{51} (d/4.8 \text{ kpc})^2 (n/1 \text{ cm}^{-3})^{-1}$  ergs with  $\Gamma_p = 2.3$ . The obtained  $W_p$  indicates that a molecular cloud might be associated to satisfy the hadronic scenario for the energetics. Extending this to include an estimation of the emission from secondary electrons will provide a tighter solution for hadronic scenario. For the PWN scenario, we discussed both leptonic and hadronic processes. We confirmed that the leptonic model with a time-dependent rate of electron-injection while considering the braking effect for the spin-down luminosity and the cooling effect due to synchrotron and IC energy losses could explain both the high TeV gamma-ray flux and the low X-ray flux. However, a quite high value for the total energy that the pulsar has lost is required for PSR B1800–21 in this model,  $E_{pwn} \sim 10^{52}$  ergs. For Suzaku Src2, we could obtain an acceptable model curve, and  $E_{pwn}$  was estimated to be  $\sim 10^{50}$  ergs with the assumption of  $\dot{E}(\tau) \sim 10^{35} \text{ ergs s}^{-1}$ . However, we need radio or X-rays observations to determine whether or not there is a pulse period in order to discuss the energetics further.

The model curves that are given in this paper indicate that *GLAST* could determine the spectral index of the accelerated particles, and further observations in the IR to UV band for a diffuse source could give a solution of the counterpart and the radiation mechanism.

The authors would like to thank B. Lott for providing us the data of *GLAST* LAT sensitivity. We also thank H. Yamaguchi for discussions on SNRs. This work was supported by a Grant-in-Aid for Scientific Research by the Japan Ministry of Education, Culture, Sports, Science and Technology (MEXT), the Australian Research Council, and the Inter-University Research Program of the Institute for Cosmic Ray Research. The work is also supported by a Grant-in-Aid for the 21st century center of excellence programs “Center for Diversity and Universality in Physics” and “Quantum Extreme Systems

TABLE 1  
SUMMARY OF DATA USED IN THE SED ANALYSIS.

Instrument	Source name	Symbol	Reference
VLA and other radio	G8.7–0.1	filled circle	(1)
VLA	G8.31–0.09	open circle	(2)
<i>Suzaku</i> XIS	Suzaku Src1	closed region (dashed)	(3)
<i>Suzaku</i> XIS	Suzaku Src2	closed region (dot-and-short dashed)	(3)
<i>Suzaku</i> XIS	diffuse UL (90% C.L.)	arrow (dashed)	(3)
<i>Chandra</i> ACIS	Suzaku Src2	closed region (dot-and-long dashed)	(4)
<i>Chandra</i> ACIS	PWN of PSR B1800–21	closed region (solid)	(5)
<i>Chandra</i> ACIS	diffuse UL	arrow (dotted)	(4)
<i>INTEGRAL</i> IBIS	Upper limit	arrow (cross)	(4)
<i>EGRET</i>	Upper limit	arrow (solid)	(4)(6)
<i>GLAST</i>	1 year sensitivity	dash-dot-dotted line	(7)
2MASS	NIR point UL	triangle	(8)
H.E.S.S.	HESS J1804–216	open square	(9)
CANGAROO-III	HESS J1804–216	filled square	this work

REFERENCES. — (1) Kassim & Weiler 1990b; (2) Brogan et al. 2006; (3) Bamba et al. 2007; (4) Kargaltsev et al. 2007b; (5) Kargaltsev et al. 2007a; (6) Hartman et al. 1999; (7) *GLAST* LAT 2007; (8) Skrutskie et al. 2006; (9) Aharonian et al. 2006a

TABLE 2  
SUMMARY OF PARAMETERS USED IN THE  
LEPTONIC MODEL SHOWN IN FIG. 6.

$\Gamma_e$	2.5	2.0	1.0
$E_{max,e}$ [TeV]	3.6	2.3	1.3
$W_e$ [ $10^{48}$ ergs]	330	17	1.4
Upper limit of B [ $\mu$ G]	1	8	50

TABLE 3  
SUMMARY OF PARAMETERS USED IN THE  
HADRONIC MODEL.

$\Gamma_p$	2.3	2.0	1.5	1.0
$E_{max,p}$ [TeV]	30	16	7.9	5.4
$W_p^a$ [ $10^{51}$ ergs]	9.3	3.1	1.3	0.96
$W_p^b$ [ $10^{51}$ ergs]	5.9	2.0	0.84	0.61

<sup>a</sup> For SNR G8.7–0.1,  $d = 4.8$  kpc.

<sup>b</sup> For PSR B1800–21,  $d = 3.84$  kpc.

TABLE 4  
BRAKING INDEX DEPENDENCE OF THE  
PARAMETERS.

braking index	$E_{pwn}$ [ergs]	$P_0$ [ms]
3	$2.6 \times 10^{49}$	210
2.5	$5.8 \times 10^{49}$	120
2.2	$1.3 \times 10^{50}$	72
1.8	$1.2 \times 10^{51}$	19
1.6	$1.3 \times 10^{52}$	5.2
1.4	$1.7 \times 10^{54}$	0.37

and their Symmetries” from MEXT of Japan. We thank the Defense Support Center Woomera and BAE systems, and acknowledge all of the developers and collaborators on the GALPROP project. Y. Higashi and T. Nakamori were supported by Japan Society for the Promotion of Science Research Fellowships for Young Scientists.

## REFERENCES

- Aharonian, F. A., et al. 2005a, *Science*, 307, 1938  
 Aharonian, F. A., et al. 2005b, *A&A*, 442, L25  
 Aharonian, F. A., et al. 2006a, *ApJ*, 636, 777  
 Aharonian, F. A., et al. 2006b, *A&A*, 448, 43  
 Altenhoff, W. J., Downes, D., Pauls, T., & Schraml, J. 1978, *A&AS*, 35, 23  
 Bamba, A., et al. 2007, *PASJ*, 59, S209  
 Blitz, L., Fich, M., & Stark, A. A. 1982, *ApJS*, 49, 183  
 Blondin, J., Chevalier, R., & Frierson, D. 2001, *ApJ*, 563, 806  
 Briskin, W. F., Carrillo-Baragan, M., Kurtz, S., & Finley, J. P. 2006, *ApJ*, 652, 554  
 Brogan, C. L., Gelfand, J. D., Gaensler, B. M., Kassim, N. E., & Lazio, T. J. 2006, *ApJL*, 639, L25  
 Clifton, T. R., & Lyne, A. G. 1986, *Nature*, 320, 43  
 Cordes, J. M., & Lazio, T. J. W. 2002, *astro-ph/0207156*  
 Cramphorn, C. K., & Sunyaev, R. A. 2002, *A&A*, 389, 252  
 Cui, W., & Konopelko, A. 2006, *ApJ*, 652, L109 (erratum 2007, *ApJ*, 665, L83)  
 Enomoto, R., et al. 2002, *Astropart. Phys.*, 16, 235  
 Enomoto, R., et al. 2006a, *ApJ*, 638, 397  
 Enomoto, R., et al. 2006b, *ApJ*, 652, 1268  
 Fatuzzo, M., Melia, F., & Crocker, R. M. 2006, *astro-ph/0602330*  
 Finley, J. P., & Ögelman, H. 1994, *ApJ*, 434, L25  
 Fisher, R. A. 1936, *Annals of Eugenics*, 7, 179  
 Frail, D. A., Kassim, N. E., & Weiler, K. W. 1994, *AJ*, 107, 1120  
 Funk, S., Hinton, J. A., Pühlhofer, G., Aharonian, F. A., Hofmann, W., Reimer, O., & Wagner, S. 2007, *ApJ*, 662, 517  
*GLAST* LAT Performance 2007,  
[http://www-glast.slac.stanford.edu/software/IS/glast\\_lat\\_performance.htm](http://www-glast.slac.stanford.edu/software/IS/glast_lat_performance.htm)  
 Hamilton, A. J. S., Chevalier, R. A., & Sarazin, C. L. 1983, *ApJS*, 51, 115  
 Handa, T., Sofue, Y., Nakai, N., Hirabayashi, H., & Inoue, M. 1987, *PASJ*, 39, 709  
 Hartman, R. C., et al. 1999, *ApJS*, 123, 79  
 Hillas, A. M. 1985, *Proc. 19th ICRC(La Jolla)*, 3, 445  
 Hinton, J. 2007, *arXiv.0712.3352*  
 Kabuki, S., et al. 2003, *Nucl.Inst.Meth.*, A500, 318  
 Kabuki, S., et al. 2007, *ApJ*, 668, 968  
 Kargaltsev, O., Pavlov, G. G., & Garmire, G. P. 2007a, *ApJ*, 660, 1413  
 Kargaltsev, O., Pavlov, G. G., & Garmire, G. P. 2007b, *ApJ*, 670, 643  
 Kassim, N. E., & Weiler, K. W. 1990a, *Nature*, 343, 146  
 Kassim, N. E., & Weiler, K. W. 1990b, *ApJ*, 360, 184  
 Kawachi, A., et al. 2001, *Astropart. Phys.*, 14, 261  
 Kubo, H., et al. 2001, *Proc. 27th ICRC(Hamburg)*, 2900  
 Landi, R., et al. 2006, *ApJ*, 651, 190  
 Livingstone, M. A., Kaspi, V. M., Gotthelf, E. V., & Kuiper, L. 2006, *ApJ*, 647, 1286  
 Mazzali, P. A., et al. 2006, *ApJ*, 645, 1323  
 Nishijima, K., et al. 2005, *Proc. 29th ICRC(Pune)*, 5, 327  
 Odegard, N. 1986, *AJ*, 92, 1372  
 Ojeda-May, P., Kurts, S. E., Rodríguez, L. F., Arthur, S. J., & Velázquez, P. F. 2002, *Rev.Mexicana.Astrofis.*, 38, 111

- Pacini, F., & Salvati, M. 1973, *ApJ*, 186, 249
- Pfrommer, C., Enßlin, T. A., 2004, *A&A*, 413, 17
- Porter, T. A., & Strong, A. W. 2005, *Proc. 29th ICRC(Pune)*, 4, 77
- Reich, W., Fürst, E., Steffen, P., Reif, K., & Haslam, C. G. T. 1984, *A&AS*, 58, 197
- Sedov, L. I. 1959, *Similarity and Dimensional Methods in Mechanics*, New York; Academic Press
- Skrutskie et al. 2006, *AJ*, 131, 1163
- Strong, W. S., & Moskalenko, I. V. 2006, GALPROP project, [http://galprop.stanford.edu/web\\_galprop/galprop\\_home.html](http://galprop.stanford.edu/web_galprop/galprop_home.html)
- Taylor, J. H., & Cordes, J. M. 1993, *ApJ*, 411, 674
- White, R. L., Becker, R. H., & Helfand, D. J. 2005, *AJ*, 130, 586
- Yamazaki, R., Kohri, K., Bamba, A., Yoshida, T., Tsuribe, T., & Takahara, F. 2006, *MNRAS*, 371, 1975